

Augmented Signal Processing in Liquid Argon Time Projection Chamber with Deep Neural Network

H. W. Yu,^{a,1} M. Bishai,^a W. Q. Gu,^a M. F. Lin,^b X. Qian,^a Y. H. Ren,^b A. Scarpelli,^a B. Viren,^a H. Y. Wei,^a H. Z. Yu,^c K. Yu,^b C. Zhang^a

^a*Physics Department, Brookhaven National Laboratory, Upton, NY, USA*

^b*Computational Science Initiative, Brookhaven National Laboratory, Upton, NY, USA*

^c*Sun Yat-Sen (Zhongshan) University, Guangzhou, China*

E-mail: hyu@bnl.gov

ABSTRACT: Liquid argon time projection chamber (LArTPC) is an advanced neutrino detector technology widely used in recent and upcoming accelerator neutrino experiments. It features a low energy threshold and a high spatial resolution allowing for a comprehensive reconstruction of event topology. In the current-generation LArTPC, the recorded data consists of digitized waveforms on wires produced by induced signal of drifting ionization electrons, which can also be viewed as 2-dimensional (time versus wire) projection images of charged-particle trajectories. For such an imaging detector, a critical step is the signal processing that reconstructs the original charge projections from the recorded 2D images. For the first time, we introduce a deep neural network (DNN) in LArTPC signal processing to improve the signal region of interest (ROI) detection. By combining domain knowledge (e.g. matching information from multiple wire planes) and deep learning, this method shows a significant improvements over traditional methods. In this paper, we report details of the method, software tools, and performance evaluated with realistic detector simulation.

KEYWORDS: LArTPC, Signal Processing, Wire-Cell, Deep Neural Network

¹Corresponding author

Contents

1	Introduction	1
2	LArTPC Signal Processing	4
3	Deep Neural Network ROI Detection	5
3.1	Neural Network Architecture	5
3.2	Usage of Geometry Information	6
3.3	Simulation, Data Pre-processing, and Truth Label Preparation	8
3.4	Network Training	9
4	Performance and discussions	9
5	Summary	12
A	Fast Projection using the Ray Grid technique	14

1 Introduction

Liquid Argon Time Projection Chamber (LArTPC) is a key detector technology for many current and future accelerator neutrino experiments [1–4]. When charged particles transverse through the LAr medium, both scintillation light and ionization electrons are created. While the detection of scintillation light provides the event time, the detection of ionization electrons provides high-resolution position and energy information of particle trajectories. The rich event topology information provided by LArTPC carries unique advantages in performing electron-photon separation. Together with the superior calorimetry capability, LArTPC is an excellent detector to study ν_μ to ν_e oscillations, which may hold the key to answer some of the remaining questions in the neutrino sector [5].

The current-generation LArTPCs are typically equipped with wire readouts that is being developed rapidly [6], instead of pixelated readouts, under the consideration of cost and heat production of electronics inside LAr [7]. In this configuration, the anode typically consists of multiple (commonly three) wire planes with different wire orientations. Under an uniform external electric field, the produced ionization electrons drift towards the anode planes at a (known) constant speed. The arrival time of ionization electrons, combined with the event time provided by the light detection system, allows for a position reconstruction of activities along the electric field. The combination of wire signals from different planes provides the position information perpendicular to the electric field. Together, 3D reconstruction of activities inside LArTPC can be made. In order to realize this concept, the wire planes with different orientations must record signals from the same ionization electron cloud multiple times. This is achieved by using both induction and

collection wire planes. By properly configuring the electric fields between wire planes, the ionization electrons can fully pass through the first few (induction) wire planes, and then get collected by the last (collection) wire plane. When ionization electrons move close to the wires, induced current can be detected. As governed by the Ramo's theorem [8], the induced current has bipolar and unipolar shapes on the induction-plane and collection wires, respectively. While the signal reconstruction for the collection-plane wires is generally simpler, it is more complex for the induction-plane wires given the potential large cancellation effect of the bipolar signals. In this work, we introduce a novel signal processing procedure utilizing modern deep-learning techniques and assisted by correlating information from multiple planes. This new procedure leads to an improved reconstruction of ionization electron distributions, which further enhances the quality of overall event reconstruction.

The recorded digitized TPC signal is a convolution of the distribution of the arriving ionization electrons and the impulse detector response:

$$M(t, x) = \int_{-\infty}^{\infty} \int_{-\infty}^{\infty} R(t - t', x - x') \cdot S(t', x') dt' dx' + N(t, x) \quad (1.1)$$

where $M(t, x)$ is a measurement, such as an ADC value at a given sampling time and wire position; $R(t - t', x - x')$ is the impulse detector response including both the field response, which describes the induced current by a moving ionization electron, and the electronics response from the shaping circuit; $S(t', x')$ is the charge distribution in time and space of the arriving ionization electrons; $N(t, x)$ is the electronics noise. The goal of the TPC signal processing is to reconstruct the original charge distribution S from the measurement M given the known detector response R in the presence of the electronics noise N .

Developed upon earlier work in Ref. [9], the current state-of-art algorithm to reconstruct the original ionization electron distribution is the so-called "2D deconvolution" technique [10, 11] utilizing the Discrete Fourier Transformation. This TPC signal processing algorithm is implemented in the *Wire-Cell Toolkit* [12] and can be run as a plug-in of the LArSoft software suite [13]. Although this algorithm has shown good performance and is adopted in many experiments, there are still room to improve, especially for tracks that has large angle with respect to the wire orientation. This type of tracks are known as the "prolonged tracks" since they induce current on a given wire over an extended period of time [10]. Figure 1 illustrates the challenge in signal processing for prolonged tracks (with a 80°track angle). In this paper, the track angle is defined by the track projection on a 2D plane, in which the x-axis is the wire pitch direction and y-axis is the electron drifting direction. The track angle is measured by the angle between track projection and the x-axis in this plane, defined as θ_{xz} . This angle definition is the same as used in figure 8 of Ref. [10].

While the TPC signals for a track with a $\theta_{xz} = 45^\circ$ are clear (see. figure 1), the ones for a track with $\theta_{xz} = 80^\circ$ are rather weak. Such a big difference with respect to the track angle is the result of the bipolar and long-range nature of the induced current for a point source on the induction-plane wires. A prolonged track thus leads to large cancellation of the induced current resulting in a low signal to background ratio. The same conclusion can be drawn viewing from the frequency domain. First, the average response function of the induction-plane wires must approach to zero at low frequency (see e.g. figure 12 of [10]), since the net charge collected on an induction-plane wire is zero [8]. Second, the signal of a prolonged track mostly resides at low frequency. Therefore, the measured signal strength, which is the product of signal strength of a prolonged track

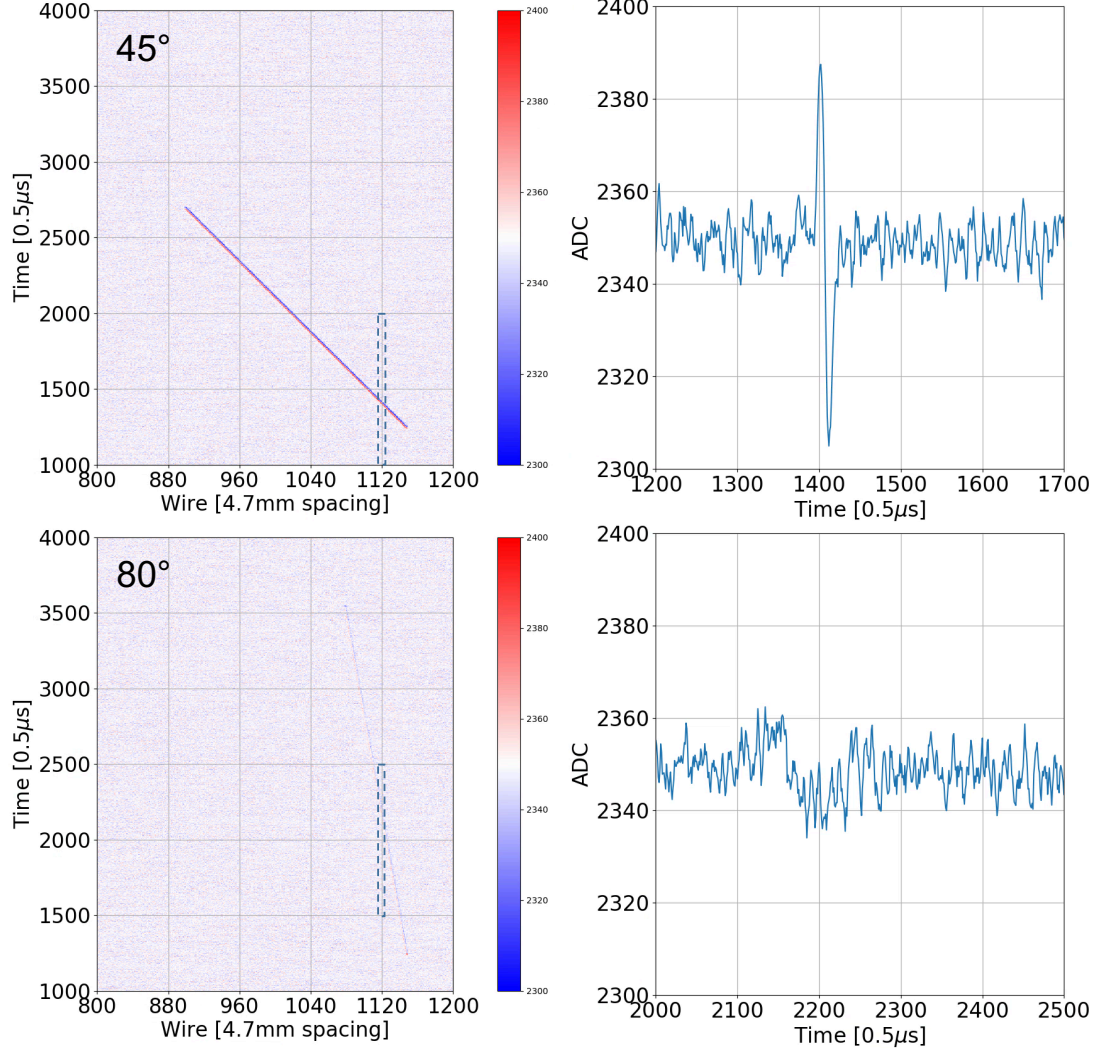


Figure 1: Left: projection of a minimum ionizing particle (MIP) track on one induction plane; right: a section of waveform of wire 1120 from the left plot indicated by the dashed box. Track angle projected on this plane is 45° (Top) and 80° (Bottom) with respect to the wire orientation. The recorded signal for the 80° track is weak as the result of the cancellation effect of the bipolar field response and the extended (in time) distribution of ionization electrons.

and the average response function, can become small compared with the low-frequency electronics noise leading to a poor signal to noise ratio. In order to achieve a good performance of the signal processing, Ref. [10] introduced a region of interest (ROI) detection technique, whose goal is to define a ROI in the time domain to contain the distribution of ionization electrons. The ROI significantly reduces low-frequency noise for the induction planes, which in turn increases the signal-to-noise ratio. Obviously, to maximize the signal-to-noise ratio, the ROI fully containing the distribution of ionization electrons in the time domain should be as small as possible. For this reason, the ROI finding algorithm in Ref. [10] worked on the deconvolved waveform instead of the raw waveform, since the ROI found in the latter case is typically bigger as a consequence

of the extended detector response. With a set of heuristic logic, the ROI searching algorithm in Ref. [10] further utilizes the connectivity information of ROIs on adjacent wires in a wire plane to enhance ROI detection efficiency, since the TPC signals tend to be continuous for any charged particle track. Note, while the ROI detection is crucial for the induction-plane signal processing, it is less important for collection-plane, where the field response is generally unipolar.

However, even with the usage of "2D deconvolution" technique and "connectivity" information, some TPC signals, e.g. prolonged tracks, are still hard to identify. Adding more information progressively into the heuristic logic of the ROI detection algorithm [10] is not an scalable approach. We thus propose a novel LArTPC signal processing procedure based on the Deep Neural Network (DNN). DNNs are known to be able to handle complicated correlations and covers solution phase space more efficiently. In the field of high-energy physics, there are many successful applications of DNN (see Refs. [14–18] among others). Furthermore, inspired by the *Wire-Cell* imaging concept in Ref. [19], the TPC signals from other wire planes can be used to enhance the ROI detection efficiency through utilizing the geometry information from multiple wire planes. Combining machine learning and domain knowledge, the new DNN LArTPC signal processing shows significantly improved performance especially for prolonged tracks.

This paper is organized in the following. The current state-of-art signal processing is briefly reviewed in section 2. The new DNN signal processing is introduced in section 3. The architecture of the DNN, the *Wire-Cell* imaging concept, the simulation and data pre-processing, and the network training are described in section 3.1, section 3.2, section 3.3, and section 3.4, respectively. The performance evaluation of the DNN signal processing is presented in section 4 followed by a summary in section 5.

2 LArTPC Signal Processing

As introduced in section 1, LArTPC signal processing extracts ionization charge distribution as a function of drift time and wire number from the induced current on the readout wires. Figure 2 shows a simplified flowchart of the state-of-art signal processing algorithm in Refs. [10, 11].

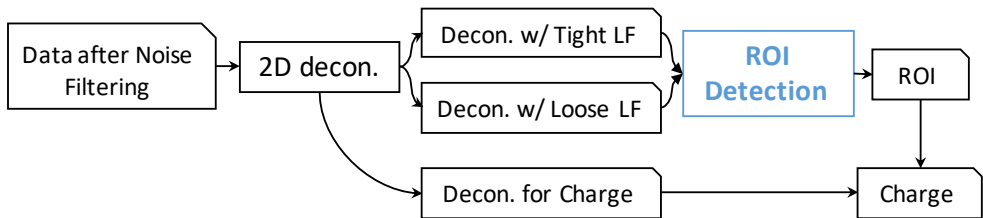


Figure 2: Flowchart of the LArTPC signal processing algorithm in Ref. [10]. "LF" stands for low-frequency software filter. "Decon." stands for deconvolution.

Starting from noise-filtered waveform [20], several 2D deconvolutions are performed with different software filters in the frequency domain. Each deconvolution follows Eq. 2.1 resolving the signal S using measurement M and detector response R in the frequency domain. A follow-up Inverse Fourier Transform (*IFT*) converts the signal S back to time and space domain. Software filters (F) in the frequency domain are used to suppress noise at high and/or low frequencies. Here, the

low-frequency filter is necessary (not used) to process signals in the induction-plane (collection-plane) wires, as the bipolar nature of field response of induction-plane wires suppresses signals at low frequency. The different low-frequency filters have different features in the signal extraction. For example, a tight low-frequency filter limiting the band width at higher frequency value leads to a high-purity but low-efficiency signal extraction. On the other hand, a loose low-frequency filter expanding the bandwidth to lower frequency leads to a low-purity but high-efficiency signal extraction.

$$S(\omega_t, \omega_x) \sim \frac{F(\omega_t, \omega_x) \cdot M(\omega_t, \omega_x)}{R(\omega_t, \omega_x)} \xrightarrow{IFT} S(t, x) \quad (2.1)$$

With the deconvolved waveform, ROI detection is performed to identify signal regions that are more likely caused by ionization signals (instead of noise). The ROI detection step intends to open windows just large enough to contain signals in order to maximize the signal-to-noise ratio. A set of heuristic logic is implemented to detect ROIs from the deconvolved signals from loose and tight low-frequency filters based on the connectivity information. With the ROI windows defined, the waveform outside are suppressed to zero, which reduces data size significantly and makes the following reconstruction steps computationally more efficient. The detected ROIs are then applied on the deconvolved waveform without applying low-frequency filters ("Decon. for Charge" in figure 2). While the removal of the low-frequency filters minimizes the distortion on the ionization electron distribution, the application of ROIs in the time domain keep the signal-to-noise ratio high, which is important for induction-plane wires.

The goal of ROI detection is to achieve high efficiency and high purity. This could be challenging when signal-to-noise ratio is low, such as those of the prolonged tracks described in section 1. In addition, the heuristic logic in ROI detection sometimes may fail in a busy situation where a lot of activities are present (e.g. near neutrino interaction vertex or inside an electromagnetic shower). In the next section, we introduce a novel ROI detection algorithm using covolutional neural network based on information from multiple wire planes, which improves the signal processing performance significantly.

3 Deep Neural Network ROI Detection

In this section, we describe the details the Deep Neural Network (DNN) architecture, use of geometric information from multiple wire planes, the simulation and data pre-processing, and the network training.

3.1 Neural Network Architecture

To apply the DNN, the ROI detection problem is essentially labeling each pixel in a 2D image (with one dimension spanning LArTPC readout channels and the other spanning the drift time) as “signal” or “not-signal” (noise). Such a problem of dividing pixels from a picture into separated groups belongs to the class of machine learning procedures called *semantic segmentation*. We adopted the U-Net network architecture introduced by O. Ronneberger et al. [21] in 2015, which

has been developed into a family of network architectures (see Refs [17, 22] among others). The network configuration is shown in figure 3. This network consists of an initial encoding path, a final decoding path, and skip connections which bridge these first two paths at various levels. Each level contains two 3×3 convolution layers and two batch normalization layers. In the encoding path, output tensors of each level are downsampled into the next level through a 2×2 max pooling operation; in the decoding path output tensors of each level are upsampled by a bilinear upsample operation. The upsampled tensors are concatenated with tensors copied from the same level of the encoding path to form input for each level of the decoding path. The encoding path finds patterns at different levels based on the original information from input channels. In the decoding path, output channels are reconstructed from the patterns found from deeper level or from the skip connections. In the application of ROI detection, we use a 5-level network. After a factor of 2 condensing in the height and width dimensions and in the deepest level of the network, pattern recognition is effectively performed in regions of $48 (= 3 \times 2^4) \times 48$ pixels.

3.2 Usage of Geometry Information

In a LArTPC with multiple wire planes, each ionization electron is independently sensed by each wire plane. Therefore, we can use the information from the other wire planes to assist ROI detection in the targeted wire plane through correlating the geometric relation among wires with different orientations. Such geometric constraints are expected to be more efficient for LArTPCs with three or more wire planes. As an example, we use a three-plane configuration with the first two induction planes labeling as U and V and the final collection plane labeling as W. This idea of *multi-plane constraint* in signal processing is inspired by the *Wire-Cell* tomographic reconstruction technique from Ref. [19]. The procedure of implementing geometric constraints on the induction-plane wires is described below and illustrated in figure 4:

1. For each channel, initial signal ROIs are formed by combining the deconvolved signals with tight and loose low-frequency software filters (see figure 2). The combination utilizes the connectivity information but skips the majority of heuristic logic in refining ROIs.
2. Across the channels, these initial signal ROIs are sliced into contemporaneous time slices of fixed duration (e.g., four time ticks or two μs). Such a choice ensures negligible loss of the information following the Nyquist sampling theorem.
3. In a given time slice, we determine a subset of channels from each plane consisting of those which are inside initial signal ROIs.
4. For each induction-plane channel inside the subset, we determine if any of its wires overlap with two wires from the other two subsets (one from each) *. The successfully matched channels are referred to as the *three-plane coincidence* (MP3).
5. For each induction-plane channel outside the subset, we determine if any of its wires overlap with two wires from the other two subsets (one from each). The successfully matched channels are referred to as the *two-plane coincidence* (MP2).

*In the case of wrapped wires, one channel may correspond to multiple wires.

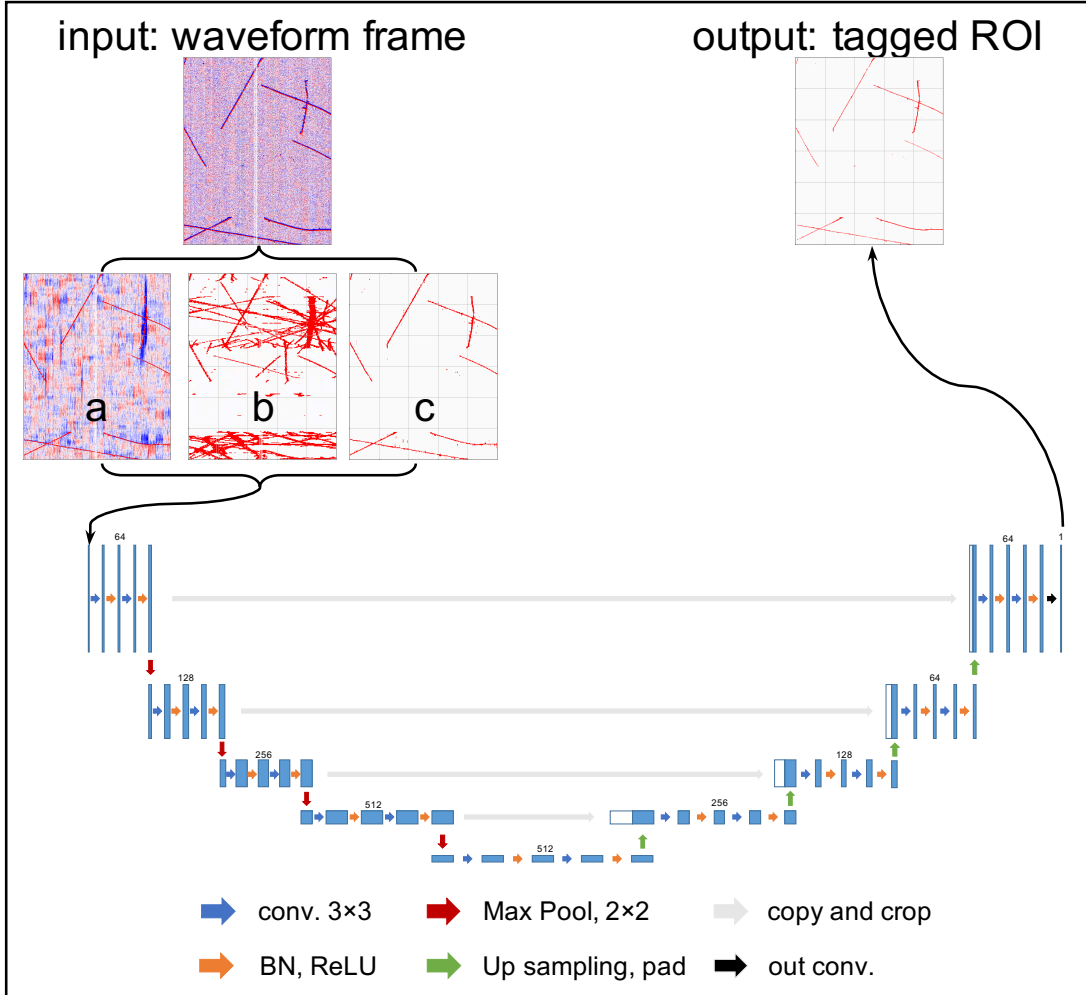


Figure 3: U-Net architecture used in the ROI detection for the DNN LArTPC signal processing. Intermediate 2D images are generated from original images containing raw waveform. Several of these intermediate images are stacked to a multi-channel 2D image serving as the input of the U-Net. Numbers of intermediate images can be varied. In this example, three are used: a) deconvolved signals from a loose low-frequency filter; b) MP2, and c) MP3. Output of the U-Net is a single channel 2D image labeling each pixel as signal (i.e. inside ROI) or not.

6. The above three steps are repeated for every time slice.

Identifying the coincidence (MP2 or MP3) is a combinatorial problem with the potential to require prohibitive computational expense. To combat this we developed an optimization technique for the primitive operations used to determine wire overlap by exploiting the symmetries of uniform wire direction and pitch. More details can be found in appendix A.

As shown in figure 3, three 2D images are used as input to the DNN to detect ROI for each induction wire plane. The first image is the deconvolved result after applying the loose low-frequency software filter. The content in each 2D pixel (one channel and one time tick) is a float number representing the reconstructed ionization charge. The second image is the result of MP2.

The content in each pixel is a number with the Boolean type, with unity (zero) labeling the pixel to be inside (outside) the MP2. The last image is the result of MP3 also with Boolean type. Although MP2 and MP3 are obtained after rebinning four time ticks into one time slice, it is straight forward to determine if one pixel with one time tick is inside the MP2 or MP3 region. An example of these arrays is shown in figure 5.

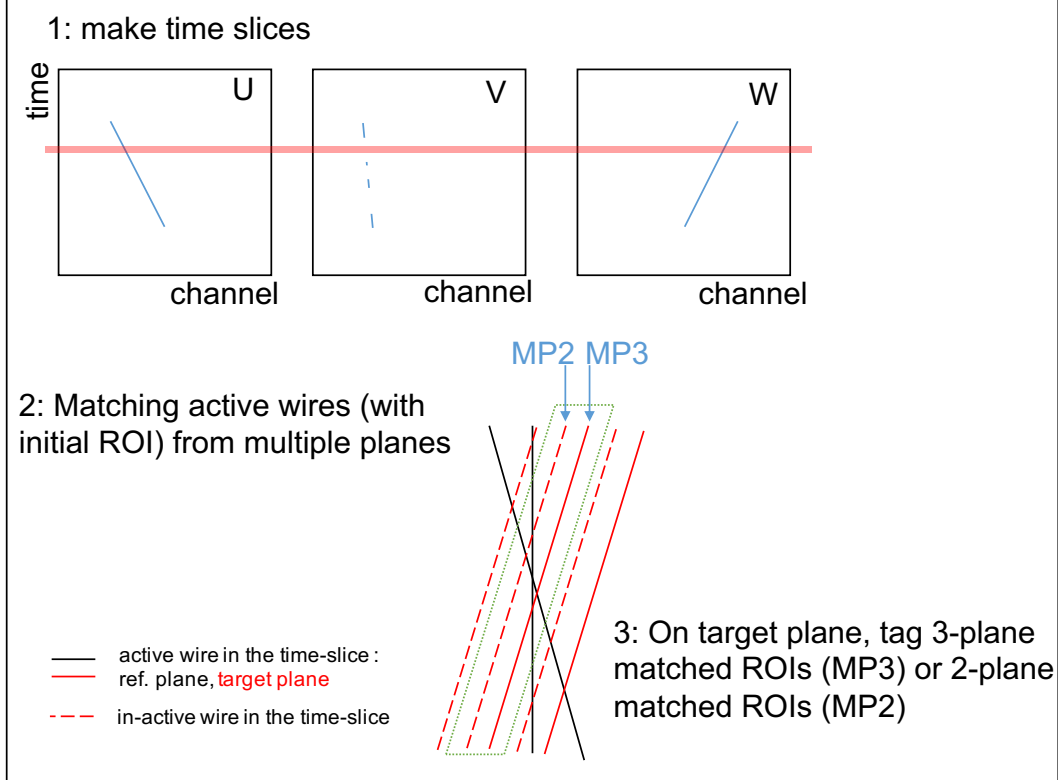


Figure 4: Illustration of creating MP2 and MP3 images. The application of geometric constraints is performed at each time slice (four time ticks).

3.3 Simulation, Data Pre-processing, and Truth Label Preparation

The data samples used to train the network are generated from a comprehensive and detailed simulation over multiple stages of physics. These begin with an initial sampling of kinematics from cosmic ray muon models [23], particle passage through detector material and the resulting energy depositions [24], the production of electrons including recombination effects [13], and the detector signal and noise simulation [12]. The detector response in the last step is provided by the *Wire-Cell Toolkit* including the ionization electron drift, diffusion, stochastic fluctuations, field response, and electronics response. The data pre-processing steps includes i) excess noise filtering, ii) initial deconvolution, iii) initial ROI finding. The excess noise filtering is particularly crucial in dealing with real detector data, but less important for simulation. The initial deconvolution and ROI finding are discussed in section 3.2. More details can be found in Ref. [25]. The simulation and data pre-processing chain is validated with ProtoDUNE Single Phase detector as described in Ref. [26].

The input to DNN consists of MP2 (figure 5c), MP3 (figure 5d), and deconvolved signals from a loose low-frequency filter (figure 5b). Note, MP2 and MP3 are generated from the deconvolved signals with a tight (figure 5a) and a loose low-frequency filters. For each event sample, there are a total of 6000 time ticks covering 3 ms drift time. The number of channels are 800, 800, and 960 for induction U, induction V, and collection W planes, respectively. The average number of cosmic tracks is about 11 per event. In order to limit the usage of memory, 10 time ticks are rebinned into one time bin, which limit the typical data size of the induction plane to 600 (time bins) and 800 (channels). For any 2D image, the content value in each rebinned pixel is taken to be the average of the original value in 10 pixels (e.g. number of electrons for the deconvolved signal and 0 or 1 for MP2 and MP3). While the number of ticks used in this rebinning process could be further optimized, such a rebinning choice has a minimal impact on the ROI detection, since majority of the ROIs (>95%) have a length longer than 10 time ticks. For the network training purpose, the *truth* label is created by applying a simple ideal-detector model to the initial simulated ionization electron distributions (a smearing with Gaussian distribution). A threshold is applied on the charge of a rebinned pixel (one channel and one time bin covering 10 time ticks) to determine if a rebinned pixel contributes to an ROI. In particular, the threshold is chosen to be 100 electrons on the average charge per time tick in a rebinned pixel. Such a value is much lower than the equivalent noise charge (ENC) from the entire electronics readout chain, which is typically above 400 electrons per time tick. The average number of (true) ROIs in an induction plane is about 3500 per event. Figure 5(e) shows an example of the truth label.

3.4 Network Training

The network and supporting utilities are implemented using PyTorch [27] and are publicly accessible in Ref. [28]. We trained the network on a platform with Intel i9-9900K CPU and NVIDIA 2080 Ti GPU with 11 GB VRAM [29]. A training epoch consists of a total of 500 event samples (450 for training and 50 for validation purpose) and requires six minutes on this platform. Each sample consists of one tensor holding the binary “signal”/“not-signal” truth label elements and a second tensor holding a vector with length three (deconvolved signal with loose low-frequency filter, MP2, and MP3). With the cosmic ray simulation, each sample contains about 5 to 20 cosmic rays resulting in an average of 3500 ROIs per sample. We use binary cross-entropy [30] as the loss function and stochastic gradient decent [31] with momentum 0.9 and learning rate 0.1 as the optimizer. In next section, we evaluate the improved performance of DNN ROI detection.

4 Performance and discussions

The performance of the trained network with simulation is evaluated firstly focusing on the more challenging cases of the ideal (large-angle) prolonged tracks. For each 3D track, two projection angles ($\theta_{xz}(V)$ and $\theta_{xz}(U)$ with respect to V and U wire planes, respectively) are used to describe its 3D direction. A larger projection angle with respect to a wire plane means a longer ROI in time, which is more challenging to detect. Two metrics are used to evaluate the performance with the rebinned pixels. (rebinned) Pixel-wise efficiency is defined as:

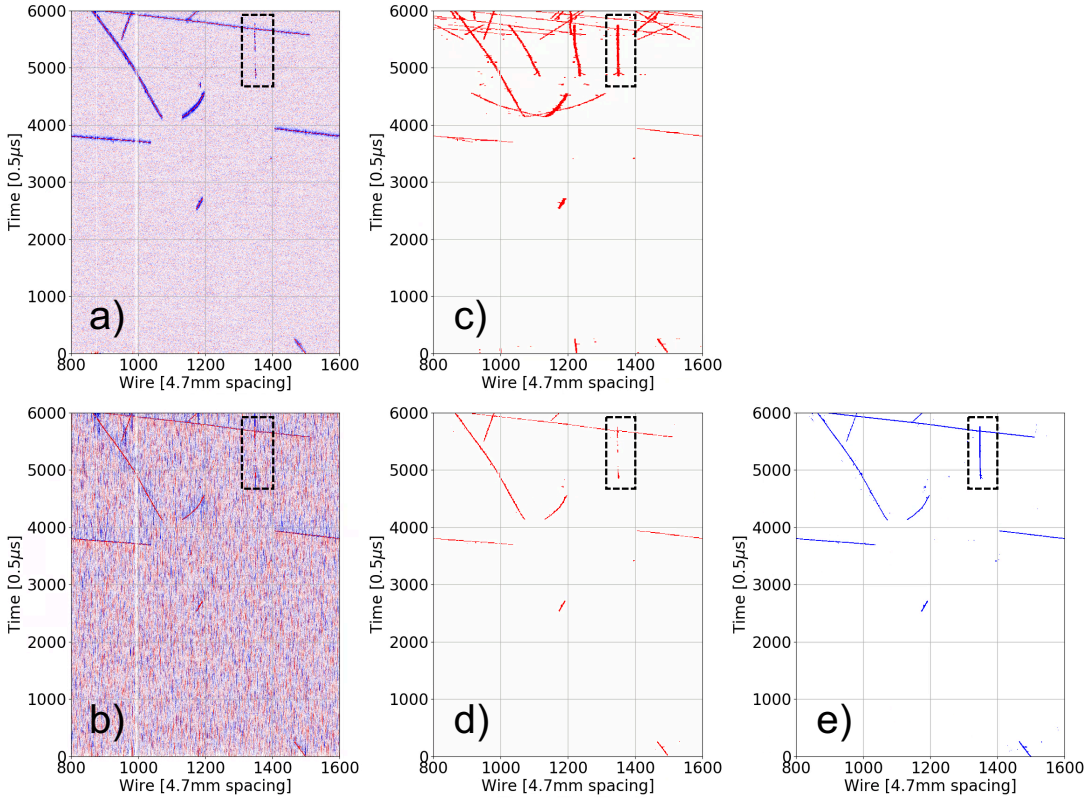


Figure 5: Example neural network input channels obtained from cosmic ray simulation for an induction wire plane. a) deconvolved image with a tight low-frequency filter; b) deconvolved image with a loose low frequency filter; c) multi-plane 2-plane coincidence (MP2); d) multi-plane 3-plane coincidence (MP3); e) truth information. Here, the deconvolved images with tight and loose low-frequency filters from different wire planes are used to produce the MP2 and MP3 images. The displayed images are with the original binning of 6000 time ticks and 800 channels. A prolonged track is indicated by the black rectangle dashed line. The input to DNN consists of b), c), and d).

$$\text{Pixel Efficiency} := \frac{\# \text{ of correctly label pixels}}{\# \text{ of ROI pixels from truth label}}. \quad (4.1)$$

Pixel-wise purity is defined as:

$$\text{Pixel Purity} := \frac{\# \text{ of correctly label pixels}}{\# \text{ of ROI pixels from reconstruction}}. \quad (4.2)$$

In this evaluation, induction V wire plane is shown as an example. Figure 6 compares pixel-wise ROI detection efficiency and purity for three algorithms: 1) current state-of-the-art ROI detection algorithm from Ref. [25] as the reference, 2) DNN ROI detection without the multi-plane geometry information, and 3) DNN ROI detection with the multi-plane geometry information. A clear improvement can be seen for the DNN ROI detection algorithm:

1. The DNN ROI detection algorithm outperforms the reference algorithm especially for extreme large-angle tracks ($> 85^\circ$).

2. DNN ROI without the multi-plane information performs better than reference but not as good as DNN ROI with the multi-plane information. In particular, comparing last three data points with 87° projection angle on V plane (75° , 85° , and 87° projection angles on the U plane), we conclude that the multi-plane geometry information is more effective when the projection angles on the other wire planes are small (i.e. less prolonged). In the extreme case when the track travels completely perpendicular to the anode wire planes, the projection angles would become 90° for both induction planes and the multi-plane geometry information becomes less useful.

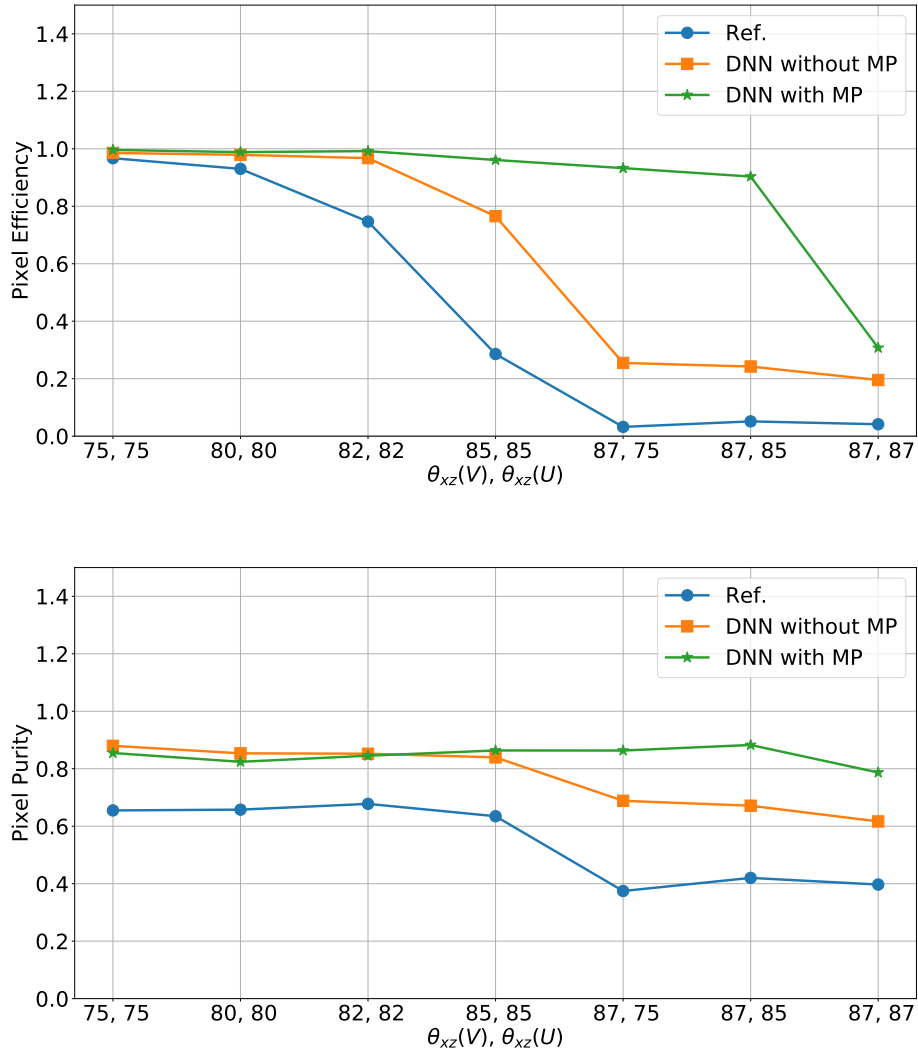


Figure 6: (rebinned) Pixel wise ROI detection efficiency and purity for 3 ROI detection algorithms evaluated using simulated prolonged tracks. X-axis is the projection angle of the track on induction V and U plane respectively in degree. ROI detection is performed on the targeted induction V plane.

The improvements of the DNN ROI detection algorithm is also shown in figure 7 with various reconstructed event images. Row (1) of figure 7 shows the reconstructed images of simulated ideal tracks with projection angles 87° on V plane and 85° on U plane for the three ROI detection algorithms (column b-d) as well as the truth label (column a). The improvements in terms of efficiency and purity numbers shown in figure 6 is self-evident. Row (2) and (3) in figure 7 show reconstructed images from simulations generated with charged pions overlaid with cosmic rays. While row (2) focuses on the reconstruction of a prolonged cosmic-ray track, row (3) focuses on a busy interaction region of a charged pion. The DNN ROI detection algorithm with multi-plane information, column (d), has the best performance among all scenarios when comparing with truth labels in column (a). The same conclusion can be drawn in applying the DNN ROI detection algorithm on the ProtoDUNE Single Phase data [32]. Preliminary results can be found in Ref. [33].

In addition to U-Net, we also implemented and evaluated two other network structures: URestNet and Nested-U-Net. URestNet [17] is U-Net with residual connections. Nested-U-Net [22] is U-Net with dense skip connections. With proper optimizations in the training, all three networks perform similarly. U-Net uses slightly less ($\sim 10\%$) GPU memory in both training and inferencing.

For a production environment with mainly C++ software stack, we implemented APIs to use TorchScript [34] in the *Wire-Cell* Toolkit [12]. The trained models are serialized in the TorchScript format. Table 1 shows a comparison of the inferencing time, memory usage, and VRAM usage among the three ROI detection algorithms.

Table 1: Comparison of resource usage for 3 ROI detection algorithms. Reference is the current ROI detection algorithm from Ref. [25]; DNN CPU/GPU: DNN ROI detection algorithm proposed in this paper, inferencing with CPU/GPU, respectively.

Method	Time per plane [sec]	Memory [GB]	VRAM [GB]
Reference	0.40	1.3	-
DNN CPU	16.7	4.8	-
DNN GPU	0.14	3.7	3.7

5 Summary

In summary, for the first time, we develop a novel DNN ROI detection algorithm for LArTPC signal processing. In this paper, we adopted the ProtoDUNE configuration in the experiment, but the generic idea and procedure should work on all types of projective wire readouts. The implementation in the *Wire-Cell* Toolkit utilizes the TorchScript APIs, which enables using trained Pytorch models in C++ production environment. This algorithm takes advantages of modern machine learning techniques as well as the domain knowledge specific to LArTPC signal processing (2-D deconvolution, multi-plane geometry correlation, etc.). Quantitative evaluations show this DNN ROI detection algorithm outperforms the current state-of-the-art ROI detection algorithm. Such improvement is expected to lead to a better reconstruction of event topology in a LArTPC, particularly for detectors having higher noise and with lower signal-to-noise ratio. (e.g. with warm electronics [3]).

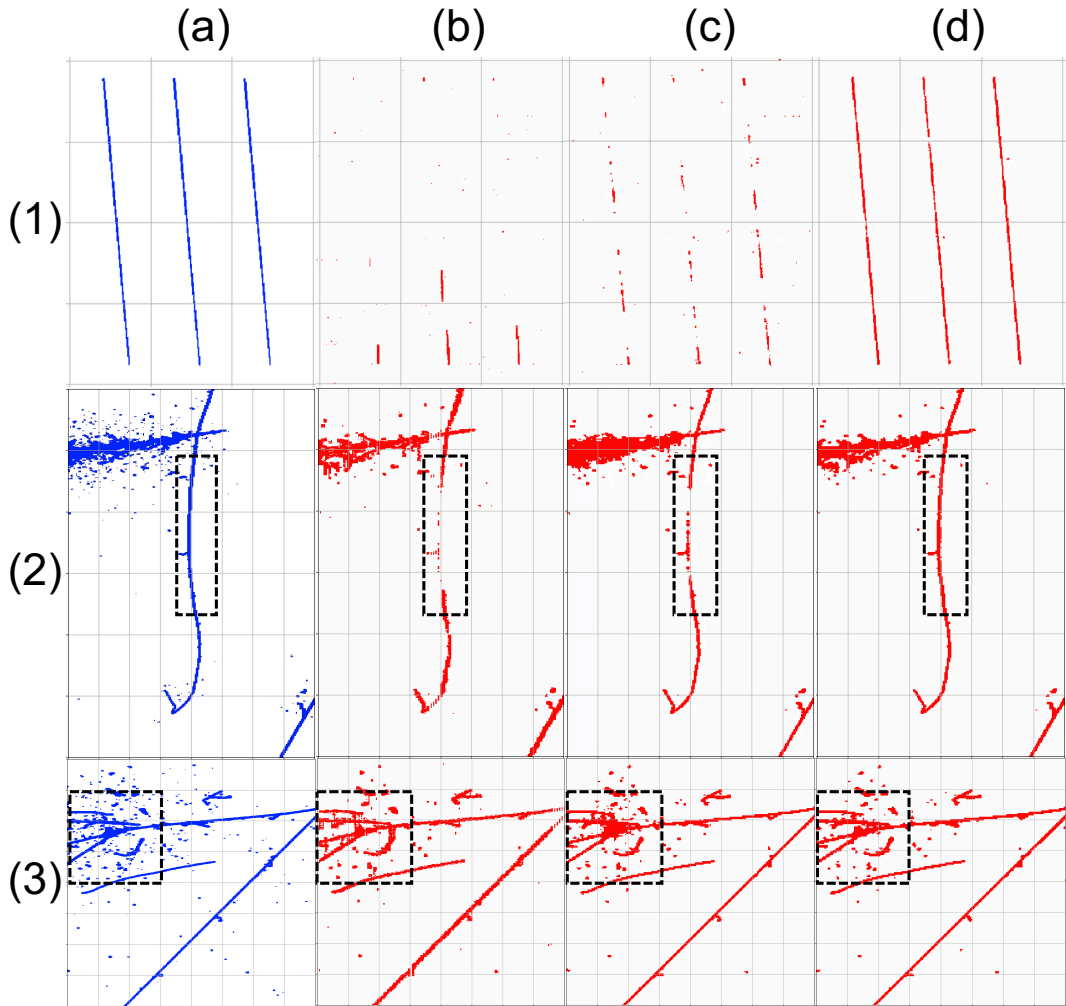


Figure 7: Event display showing the detected ROIs on different types of event topologies: (1) Ideal straight-line prolonged tracks with track angle being 87° projected to V plane and 85° projected to U plane, (2) A cosmic track with a section with a large projection angle (indicated by the black rectangle dashed line), and (3) an interaction vertex of a charged pion with many activities (indicated by the black rectangle dashed line). ROI detection is performed on V plane (target plane). The label of the columns is explained below: (a) truth label, (b) reference ROI detection algorithm [25], (c) DNN ROI detection algorithm without the multi-plane geometry information, and (d) DNN ROI detection algorithm with the multi-plane geometry information.

Acknowledgments

This work is supported by the U.S. Department of Energy, Office of Science, Office of High Energy Physics, and Early Career Research Program under contract number DE-SC0012704.

A Fast Projection using the Ray Grid technique

Central to the use of geometry information in improving signal processing efficiency as well as in the *Wire-Cell* 3D tomographic reconstruction technique [19] are a number of primitive operations which must be carried out numerous times by these higher level algorithms. Optimization of these frequently called operations is critical for the overall speed. Two core and related operations involve locating the point of intersection of a wire from each plane and then locating a wire from a third plane relative to this intersection. The so called *ray grid* method is used to optimize these operations by exploiting two symmetries of an idealized wire plane: fixed wire pitch and direction. Exploiting these symmetries transforms the problem from solving a vector equation to a simpler problem of applying indices.

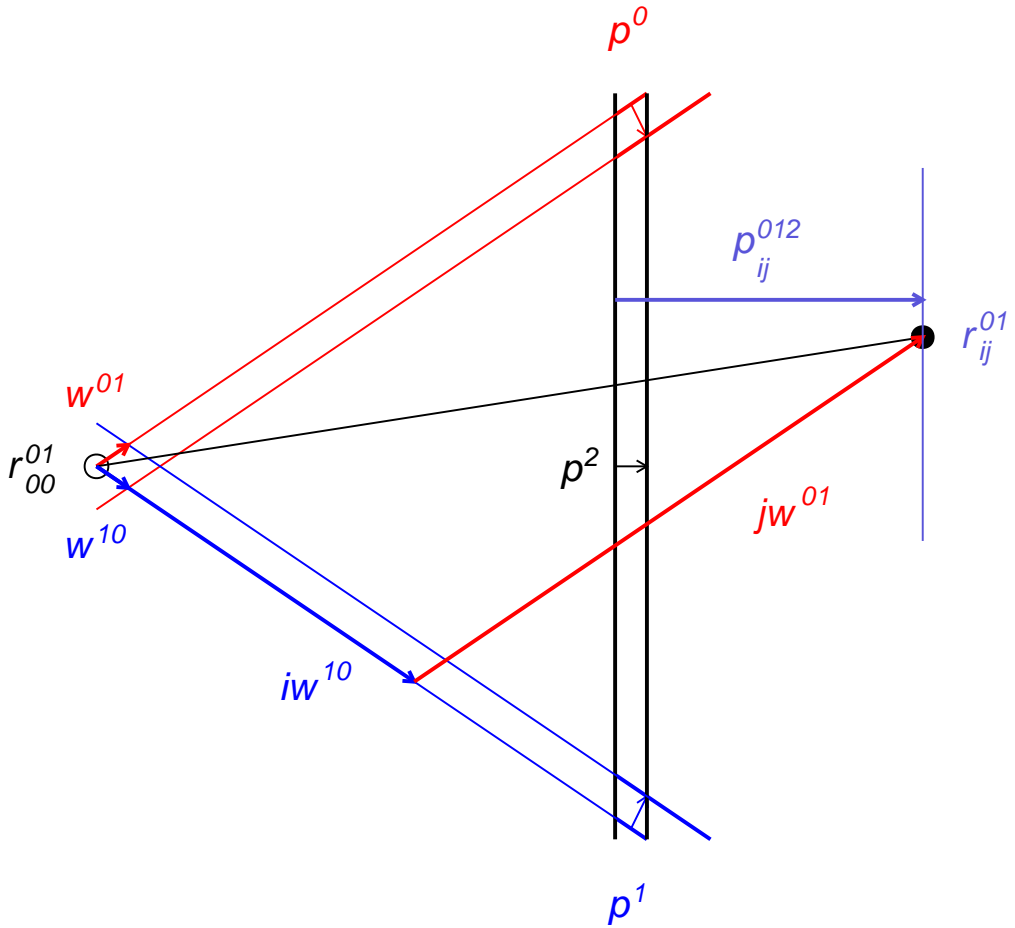


Figure 8: Example points, vectors and tensors involved in constructing and using ray grids. Layers 0, 1 and 2 are represented in red, blue and black, respectively. See text for further definitions.

With these symmetries assumed, we start by generalizing a fixed number of parallel wires in a wire plane to an infinite number of parallel rays in a *layer*. This generalization allows us to define the active area of an anode by introduce two logical layers, one providing horizontal and the other providing vertical boundaries via rays with pitch equal to the active height and width,

respectively. The higher level algorithms do not care about wires per se but about the logical lines running parallel to and half way between two neighboring wires and in so in practice we associate the abstract rays to these lines. Finally, as the higher level algorithms work in a projected space we assume all layers are co-planar which allows the problem to reduce to two dimensions.

A set of rays in a layer and their relationship to rays in a second or third layer may be categorized by a number of tensors listed below and illustrated for a three layer problem in figure 8. Within one layer we may consecutively number the rays and we mark these tensor indices with subscripts ($\in \{i, j, k\}$). We identify a special ray with an index of zero. The precise identification does not matter for the *ray grid* method. In practice the ray nearest to an edge of the active region is chosen. For quantities that span multiple layers, we mark them with superscript layer indices ($\in \{l, m, n\}$).

p^l the pitch vector for layer l gives the displacement perpendicular to the layer's rays and has magnitude that of the pitch separation of two neighboring rays.

c^n the origin vector for layer n locates the center point of the specially identified ray $i = 0$.

r_{ij}^{lm} the crossing point of ray i from layer l and ray j from layer m .

r_{00}^{lm} the crossing point the specially identified zero rays of layers l and m .

w^{lm} a vector giving the displacement along the direction of a ray in layer l between the crossing points of that ray and two neighboring rays from layer m .

The last two tensors, r_{00}^{lm} and w^{lm} can be calculated with simple vector arithmetic in a pair-wise manner among the N_l layers in the ray grid. The former is symmetric and both have undefined diagonals. These do require $O(N_l^2)$ operations where N_l is the number of layers and typically $N_l = 5$. Given these two tensors, arbitrary crossing points of rays from two different layers can be written as,

$$r_{ij}^{lm} = r_{00}^{lm} + j w^{lm} + i w^{ml}. \quad (\text{A.1})$$

By exploiting the constant ray direction and pitch, this tensor replaces numerous calls to *sin()*, *cos()* and *sqrt()* functions with multiplication, addition and array indexing.

The location of a crossing point r_{ij}^{lm} along the pitch direction of a third layer n may be written as,

$$p_{ij}^{lmn} = (r_{ij}^{lm} - c^n) \cdot \hat{p}^n. \quad (\text{A.2})$$

Expanding this in terms of r_{ij}^{lm} shows the number of unique vector operations needed to form this tensor is combinatoric in the number of layers (eg, $N = 5$) and independent from the number of wires:

$$P_{ij}^{lmn} = r_{00}^{lm} \cdot \hat{p}^n + j w^{lm} \cdot \hat{p}^n + i w^{ml} \cdot \hat{p}^n - c^n \cdot \hat{p}^n. \quad (\text{A.3})$$

Finally, the typical use of this pitch location is to identify the nearest ray in plane n by its index. This index can be found simply as,

$$I_{ij}^{lmn} = \text{floor}(P_{ij}^{lmn} / p^n). \quad (\text{A.4})$$

References

- [1] R. Acciarri et al. Design and Construction of the MicroBooNE Detector. *JINST*, 12(02):P02017, 2017, 1612.05824.
- [2] B. Abi et al. The Single-Phase ProtoDUNE Technical Design Report. 2017, 1706.07081.
- [3] M. Antonello et al. A Proposal for a Three Detector Short-Baseline Neutrino Oscillation Program in the Fermilab Booster Neutrino Beam. *arXiv:1503.01520*, 2015, 1503.01520.
- [4] Babak Abi et al. Deep Underground Neutrino Experiment (DUNE), Far Detector Technical Design Report, Volume II DUNE Physics. 2 2020, 2002.03005.
- [5] M. V. Diwan, V. Galymov, X. Qian, and A. Rubbia. Long-Baseline Neutrino Experiments. *Ann. Rev. Nucl. Part. Sci.*, 66:47–71, 2016, 1608.06237.
- [6] D.A. Dwyer et al. LArPix: Demonstration of low-power 3D pixelated charge readout for liquid argon time projection chambers. *JINST*, 13(10):P10007, 2018, 1808.02969.
- [7] Veljko Radeka et al. Cold electronics for 'Giant' Liquid Argon Time Projection Chambers. *J. Phys. Conf. Ser.*, 308:012021, 2011.
- [8] S. Ramo. Currents induced by electron motion. *Proceedings of the IRE*, 27:584, 1939.
- [9] Bruce Baller. Liquid argon TPC signal formation, signal processing and reconstruction techniques. *JINST*, 12(07):P07010, 2017, 1703.04024.
- [10] C. Adams et al. Ionization electron signal processing in single phase LArTPCs. Part I. Algorithm Description and quantitative evaluation with MicroBooNE simulation. *JINST*, 13(07):P07006, 2018, 1802.08709.
- [11] C. Adams et al. Ionization electron signal processing in single phase LArTPCs. Part II. Data/simulation comparison and performance in MicroBooNE. *JINST*, 13(07):P07007, 2018, 1804.02583.
- [12] <https://github.com/WireCell/wire-cell-toolkit>.
- [13] <http://larsoft.org/>.
- [14] A.M. Sirunyan et al. Identification of heavy-flavour jets with the CMS detector in pp collisions at 13 TeV. *JINST*, 13(05):P05011, 2018, 1712.07158.
- [15] Chase Shimmin, Peter Sadowski, Pierre Baldi, Edison Weik, Daniel Whiteson, Edward Goul, and Andreas SÅygaard. Decorrelated Jet Substructure Tagging using Adversarial Neural Networks. *Phys. Rev. D*, 96(7):074034, 2017, 1703.03507.
- [16] Peter Sadowski, Balint Radics, Ananya, Yasunori Yamazaki, and Pierre Baldi. Efficient antihydrogen detection in antimatter physics by deep learning. *J. Phys. Comm.*, 1(2):025001, 2017, 1706.01826.
- [17] C. Adams et al. Deep neural network for pixel-level electromagnetic particle identification in the MicroBooNE liquid argon time projection chamber. *Phys. Rev. D*, 99:092001, May 2019.
- [18] Pierre Baldi, Jianming Bian, Lars Hertel, and Lingge Li. Improved Energy Reconstruction in NOvA with Regression Convolutional Neural Networks. *Phys. Rev. D*, 99(1):012011, 2019, 1811.04557.
- [19] Xin Qian, Chao Zhang, Brett Viren, and Milind Diwan. Three-dimensional Imaging for Large LArTPCs. *JINST*, 13(05):P05032, 2018, 1803.04850.
- [20] R. Acciarri et al. Noise Characterization and Filtering in the MicroBooNE Liquid Argon TPC. *JINST*, 12:P08003, 2017, 1705.07341.

- [21] Olaf Ronneberger, Philipp Fischer, and Thomas Brox. U-net: Convolutional networks for biomedical image segmentation. In Nassir Navab, Joachim Hornegger, William M. Wells, and Alejandro F. Frangi, editors, *Medical Image Computing and Computer-Assisted Intervention – MICCAI 2015*, pages 234–241, Cham, 2015. Springer International Publishing.
- [22] Zongwei Zhou, Md Mahfuzur Rahman Siddiquee, Nima Tajbakhsh, and Jianming Liang. Unet++: Redesigning skip connections to exploit multiscale features in image segmentation, 2019, 1912.05074.
- [23] Ralph Engel, Dieter Heck, Tim Huege, Tanguy Pierog, Maximilian Reininghaus, Felix Riehn, Ralf Ulrich, Michael Unger, and Darko Veberić. Towards a Next Generation of CORSIKA: A Framework for the Simulation of Particle Cascades in Astroparticle Physics. *Comput. Softw. Big Sci.*, 3(1):2, 2019, 1808.08226.
- [24] S. Agostinelli et al. Geant4 – a simulation toolkit. *Nucl. Instrum. Meth.*, A506:250–303, 2003.
- [25] C. Adams, R. An, J. Anthony, J. Asaadi, M. Auger, L. Bagby, S. Balasubramanian, B. Baller, C. Barnes, G. Barr, and et al. Ionization electron signal processing in single phase larpc. part i. algorithm description and quantitative evaluation with microboone simulation. *Journal of Instrumentation*, 13(07):P07006–P07006, Jul 2018.
- [26] B. Abi et al. First results on ProtoDUNE-SP liquid argon time projection chamber performance from a beam test at the CERN Neutrino Platform. 7 2020, 2007.06722.
- [27] <https://pytorch.org>.
- [28] Haiwang Yu. Pytorch-unet for larpc signal processing.
<https://github.com/HaiwangYu/Pytorch-UNet>.
- [29] <https://www.nvidia.com/en-us/geforce/graphics-cards/rtx-2080-ti/>.
- [30] Binary Cross Entropy between the target and the output in PyTorch
<https://pytorch.org/docs/master/generated/torch.nn.BCELoss.html>.
- [31] Stochastic gradient descent (optionally with momentum) in PyTorch.
<https://pytorch.org/docs/stable/optim.html#torch.optim.SGD>.
- [32] B. Abi et al. The Single-Phase ProtoDUNE Technical Design Report. 6 2017, 1706.07081.
- [33] Haiwang Yu. Deep neural network signal processing for liquid argon time projection chamber.
<http://meetings.aps.org/Meeting/APR20/Session/X13.1>.
- [34] <https://pytorch.org/docs/stable/jit.html>.